

From Segmented Images to Physics: A Lightweight Pipeline for Transport Modeling

A. Conte^{a*}, F. Boschetti^a

a Politecnico di Milano, Department of Electronics, Informatics and Bioengineering. Milan, Italy.

* Corresponding author

Email: alessandro.conte@polimi.it

Keywords: retina; fundus image analysis; permeability mapping; albumin diffusion; porous transport.

Abstract

Clinical fundus photography is ubiquitous, fast, and inexpensive, yet its interpretation remains largely qualitative. We introduce a lightweight image-to-physics workflow that turns a single, segmented fundus image into spatially resolved biophysical inputs and model outputs relevant to retinal physiology and age-related macular degeneration (AMD). From the binary vasculature we derive local vessel radius and a permeability map that varies along each branch; an optional macular “hot-spot” represents neovascular leakage. Because capillaries are not visible in standard fundus images, we incorporate an implicit capillary correction that limits the effective exchange distance to realistic, layer-appropriate values (tighter outside the foveal avascular zone, looser within it). These maps are imported into a COMSOL transport model where vessels act as boundary sources and the retina is treated as a porous diffusive medium for albumin. We report two complementary indices on a 0–1 scale: a structural risk that reflects anatomy and material properties, and a dynamic risk that also accounts for the evolving concentration field, naturally decreasing in regions the diffusing solute has not yet reached (e.g., early times near the no-flux outer rim). Applied to real fundus geometries, the framework recovers expected trends—higher leak along thin branches, spatially heterogeneous transport around the macula—and supports sensitivity analyses over permeability, uptake, and capillary scale assumptions. The result is a reproducible, quantitative bridge between routine imaging and predictive transport modeling that can inform hypothesis testing, phenotype comparison, and scenario exploration in AMD without requiring specialized acquisitions or manual vessel labeling.

1. Introduction

Vision arises from the coordinated action of optical, neural, and fluid-transport subsystems. In the posterior eye—retina and choroid—these processes support phototransduction, metabolite exchange, and tissue homeostasis. Small disturbances in pressure or interstitial flow can therefore trigger major disease and, in extreme cases, permanent visual loss. Direct experiments are hard: deep ocular layers are delicate and difficult to access, limiting what can be measured safely in vivo [1]. Computational modeling offers a complementary route. By reproducing physiology under controlled, repeatable conditions, models help test mechanisms, interpret measurements, and inform clinical choices, aligning with the goals of precision ophthalmology [2]. This is especially pertinent for disorders driven by transport and barrier failure—glaucoma, age-related macular degeneration (AMD), diabetic macular edema, retinal detachment—where gradients, flows, and permeabilities are central to pathogenesis [3].

Retinal solute distribution depends not only on tissue properties but also on vascular architecture and endothelial leakiness [4]. In AMD, for example, neovascular complexes—choroidal or retinal (CNV)—and microvascular remodeling alter local permeability and disturb macular fluid balance. Routine fundus imaging provides a detailed map of vessel topology, yet these images are seldom converted into spatially resolved biophysical fields (e.g., diameter or permeability) that can drive forward simulations. Closing this gap would allow image-derived anatomy to directly inform predictive transport models.

Here we present a compact image-to-physics pipeline that turns a single, segmented fundus into quantitative inputs for retinal transport. First, we compute a local vessel radius map from the binary vasculature and transform it into a per-segment permeability field $P(x,y)$ via a tunable diameter–permeability relation. Second, we embed $P(x,y)$ in a COMSOL Multiphysics model: vessels act as boundary mass-transfer sources with coefficient $h_m=P(x,y)$, while the retinal parenchyma is treated as a porous diffusive medium. Third, we derive dimensionless transport metrics—Biot and Damköhler numbers—and combine them into a simple risk index that links geometry with physiology (permeability, uptake). The framework also includes an optional macular hotspot (elliptical region) to emulate CNV-like leakage and perform controlled simulations near the fovea.

The workflow is lightweight (single image), fast, and reproducible. It yields maps of diameter, permeability, effective diffusivity, and risk that can be visualized on the fundus or used directly as boundary conditions in time-dependent simulations. By coupling routine imaging with mechanistic modeling, the approach provides a practical foundation for patient-specific retinal transport studies and hypothesis testing in AMD and related macular diseases.

2. Objectives

1. Extract a robust local vessel radius $R(x,y)$ from a segmented fundus.
2. Map R into endothelial permeability $P(x,y)$ and allow a macular hotspot with elevated leak.
3. Simulate albumin transport in retinal tissue using these boundary conditions and report derived metrics (Bi , Da , $Risk$).
4. Provide verification plots and parameter choices suitable for AMD-oriented studies.

3. Methods

3.0 Motivation, data modality, and scope

Color fundus photography is among the most accessible retinal imaging modalities, yet analyses are typically qualitative. Our aim was to turn a single, pre-segmented fundus (binary: vessels vs background) into spatially resolved, physics-ready fields that can drive transport simulations relevant to macular physiology and AMD. Specifically, we sought to (i) extract local vessel radius from the network geometry, (ii) convert radius to a per-segment permeability field, (iii) account for the absence of capillaries in fundus projections by introducing an implicit capillary correction to the exchange distance [5], and (iv) embed these maps in a COMSOL Multiphysics model of albumin transport in retinal tissue. The workflow is designed to be light-weight (one image, no manual labeling beyond a single segmentation), reproducible, and compatible with time-dependent simulations. It is schematically summarized in Table 1.

Table 1. Pipeline overview: scripts, functions, and outputs

Component Step	Purpose	Main operations (conceptual)	Primary outputs
Input & scaling	Map pixels to meters; align orientation	Read binary fundus; set W,H; flip vertically to bottom-left origin	Physical grid (x,y); scaled vessel mask
Clean-up & QC	Preserve thin branches; verify mask	Light morphological bridging/closing; overlays for QC	Cleaned mask; overlay figure
Radius extraction	Compute local caliber	Internal distance transform; skeletonization; on-skeleton radius; along-skeleton smoothing; propagation to walls; in-mask smoothing	Radius map $R(x,y)$; border-only radius plot; diameter histogram
Permeability mapping	Convert caliber to leak	Monotone $R \rightarrow P$ law (bounded); optional macular ellipse with elevated leak	Permeability map $P(x,y)$ (CSV); vessel-only color map

Component Step	Purpose	Main operations (conceptual)	Primary outputs
Distance-to-vessel	Measure supply geometry	External distance transform from background to vessel walls (outside vessels); flip to physical coordinates	Distance map $\ell(x,y)$ (CSV)
Implicit capillary correction	Restore physiologic exchange length threshold	Soft FAZ window; spatial thresholds ($180\ \mu\text{m}$ / $280\ \mu\text{m}$); effective distance = $\min(\text{geometric}, \ell_{\text{eff}}(x,y))$	Effective distance
COMSOL ingestion	Use maps in a solver	Import CSVs; set porous diffusion & uptake; boundary mass-transfer with PP; closest-point projection $P \rightarrow \text{domain}$	Time-dependent concentration; boundary/source diagnostics
Indices & visualization	Summarize transport propensity	Structural risk (bounded); dynamic risk (structural \times concentration fraction); cut-lines and overlays	Risk maps (0–1); profiles; parameter sensitivities

3.1 Segmented fundus

The pipeline starts from a binary vessel map (vessels = 1, background = 0). Such a mask can be produced in several standard ways:

- (i) quick classical pipelines (green-channel extraction \rightarrow contrast normalization \rightarrow vesselness filtering/frangi or matched filtering \rightarrow adaptive thresholding \rightarrow light morphology);
- (ii) semi-automatic tools with manual proofreading;
- (iii) supervised deep networks trained on public fundus datasets.

Any of these routes yields a vessel mask suitable for our purposes because the downstream steps—radius extraction, permeability mapping, and transport modeling—are segmentation-agnostic: they only require a reasonably accurate binary topology of the larger arteriovenous tree. We therefore treat segmentation as an upstream, interchangeable module and focus the contribution on converting a given mask into physics-ready fields (radius, permeability, distance) and on the capillary-aware transport modeling that follows. In practice, we apply only light post-processing (gap bridging, minimal closing, upsampling) to stabilize skeletonization and preserve thin branches, without altering the original labeling.

3.2 Physical coordinates, scaling, and orientation

Images were mapped to a rectangular physical domain $[0,W] \times [0,H]$, with W and H chosen to represent the fundus field of view (typically 12–13 mm diameter for a 45° image). Pixel pitches in x and y were computed from (W, H) and the image resolution. Because image arrays are indexed from the top-left, all exported scalar fields were vertically flipped so that CSV coordinates follow a bottom-left origin, matching COMSOL's convention. This avoids any remapping inside the solver and ensures that locations (e.g., macula center) coincide across software.

3.3 Vessel mask pre-processing and quality control

Starting from a binary vessel mask (white vessels), we applied minimal morphological clean-up to preserve thin branches while reconnecting single-pixel gaps. Where needed, we up-sampled the image ($\times 2$) to stabilize skeletonization in very thin segments. Quality control consisted of visual overlays of the cleaned mask on the fundus and, downstream, of the check of a diameter histogram weighted by border length (to verify that small and large diameters are captured without bias).

3.4 Local radius from the medial axis

We computed the internal Euclidean distance from each vessel pixel to the closest vessel wall, and extracted the skeleton (medial axis) of the network. On the skeleton, this distance equals the local radius. To reduce noise from pixelation and bifurcations, radius values were smoothed along the skeleton (preserving topology) and then propagated from skeleton points to all in-vessel pixels by nearest-centerline labeling. A light, mask-guided smoothing inside vessels yielded a continuous radius map $R(x,y)$ down to the walls. A scalar calibration factor (near unity) can compensate for systematic

over/under-estimation if manual verifications against recognizable structures (e.g., major trunks) suggest bias.

3.5 From radius to endothelial permeability

We translated caliber into endothelial permeability under the empirical assumption that thinner branches tend to leak more. A monotone law was used to map R to P (baseline magnitude and slope chosen within physiologic ranges; upper/lower clips prevent unphysical extremes). The resulting permeability map $P(x,y)$ is defined on the vessel network and exported in physical units.

$$P(x, y) = P_0 \left(\frac{R_{ref}}{R} \right)^\alpha$$

In COMSOL, permeability acts as a boundary mass-transfer coefficient on the vessel walls, while the retinal tissue is the diffusive domain. We simulate albumin diffusion with $D_0=6 \times 10^{-11} \text{ m}^2/\text{s}$ and tortuosity $\lambda=1.6$.

3.6 Macular “hotspot” (optional CNV surrogate)

To emulate CNV-like leakage, we defined a smooth elliptical window centered on the macula. Within this region, permeability is locally elevated toward a user-set “hotspot” value; outside, it reverts to the caliber-based baseline. Only vessel segments that intersect the ellipse inherit the higher leak, reflecting the vascular origin of the source. The window is soft-edged so that transitions are gradual, avoiding numerical artifacts.

3.7 COMSOL model specification

We modeled the retina as a 2-D porous diffusive domain and the vessels as internal boundaries. Albumin transport was simulated with the Transport of Diluted Species in Porous Media interface. Diffusion used an effective diffusivity derived from free albumin diffusivity and tissue tortuosity; an optional first-order uptake provided a uniform sink. On vessel walls, we imposed External Convection (mass-transfer) with coefficient $= P(x,y)$ and blood-side concentration defined as constant.

$$n \cdot (-D_{eff} * \nabla c) = P(x, y) [conc - c]$$

The outer circular rim of the fundus was set to No Flux. Per-pixel maps (permeability, radius, distance) were imported as interpolation functions in meters and evaluated at run time. For plotting and for “structural” indices, permeability was projected from the boundary into the domain with a closest-point operator, so that each tissue location inherits the value of the nearest vessel segment.

3.8 Derived indices: structural and dynamic risk

To summarize the interplay between boundary exchange and tissue removal we reported a bounded structural risk index on $[0,1]$.

$$Risk = \frac{Bi}{(1 + Bi + Da)}$$

Where $Bi = P(x, y) * \frac{l_{eff}}{D_{eff}}$ and $Da = k * \frac{l_{eff}^2}{D_{eff}}$. The Risk increases with local permeability and effective distance to the exchanging interface and decreases with uptake. A dynamic risk multiplies the structural score by the local concentration fraction relative to the blood-side drive (clamped to 0-1). This dynamic index naturally attenuates in regions that the diffusing solute has not yet reached (e.g., early times near the no-flux rim), while converging to the structural pattern at longer times. Together, the two indices separate anatomical propensity from time-resolved availability.

$$Risk_{dyn} = Risk * c_{frac}$$

Where $c_{frac} = \min(1, \max(\frac{c}{conc}))$.

3.9 Implicit capillary modeling of exchange distance

Fundus images show arterioles and venules but not the capillary bed. In real retina, most tissue lies within $\sim 150\text{--}300\text{ }\mu\text{m}$ of a capillary (larger only within the foveal avascular zone, FAZ [6]). If the effective distance-to-vessel is computed only from large vessels, it becomes millimetric in wide areas, artificially inflating exchange metrics [7]. We therefore introduced a capillary-aware exchange distance by capping the geometric distance at a physiologic threshold: a tighter limit outside FAZ (we used $180\text{ }\mu\text{m}$) and a looser one inside FAZ (we used $280\text{ }\mu\text{m}$) via a soft elliptical window centered on the macula. The effective distance field is the minimum between the geometric distance and this spatially varying capillary scale. This “implicit capillary” assumption restores realistic length scales for exchange without explicitly segmenting capillaries and keeps the model parsimonious.

4. Results

In summary, from a segmented fundus (Figure 1), we computed a smooth local radius with medial-axis distance, regularized it along centerlines and within vessels, and converted it to permeability. We exported $P(x,y)$ as a function for boundary mass transfer in COMSOL’s TDS (porous) model of the retina, ran albumin diffusion simulations, and derived dimensionless indices (Bi , Da) and a risk map to link vascular geometry and transport physiology. The pipeline yields continuous diameter and permeability distributions: large trunks have low $P \sim 10^{-8}\text{ m/s}$, fine branches show higher $P \sim (2\text{--}6) \times 10^{-8}\text{ m/s}$, and the macular ellipse (if intersecting vessels) rises to $P_{\text{CNV}} \approx 3 \times 10^{-6}\text{ m/s}$. Time-dependent COMSOL fields show diffusion plumes emanating from high- P branches; the risk index increases with distance from vessels and permeability, and decreases with higher tissue uptake k (Figure 2).

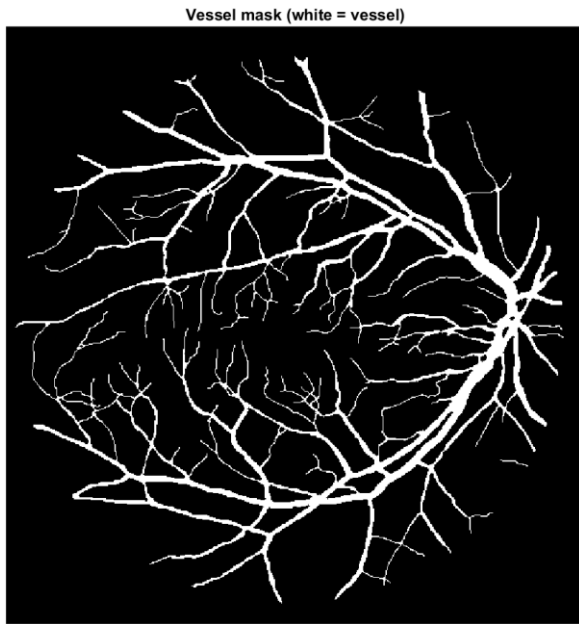


Figure 1 - Segmented fundus, starting image

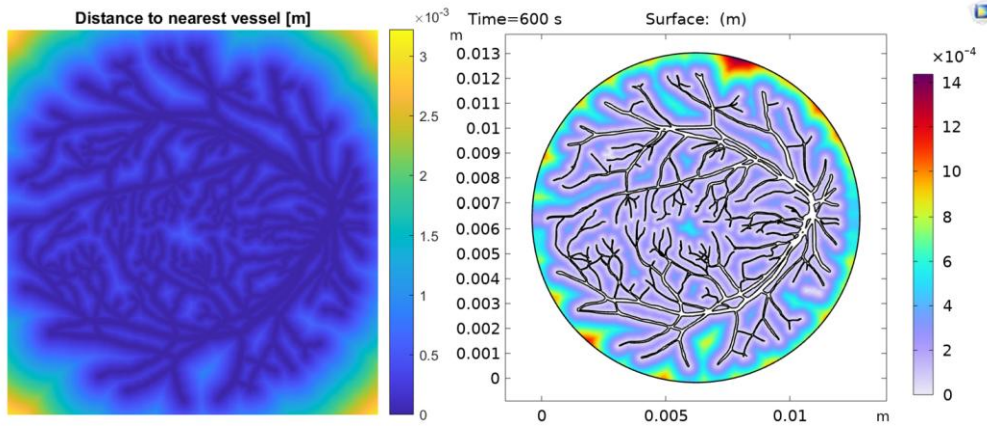


Figure 2 - Distance to nearest vessel in Matlab and Comsol

4.1 Diameter and permeability maps

The method produced a smooth map $R(x,y)$ consistent with vessel caliber: trunks $R \gg R_{ref}$ and fine branches $R < R_{ref}$. Converting to P yielded, we can recognize trunks, intermediate branches and thin branches/capillaries with an increase in permeability as in Figure 3.

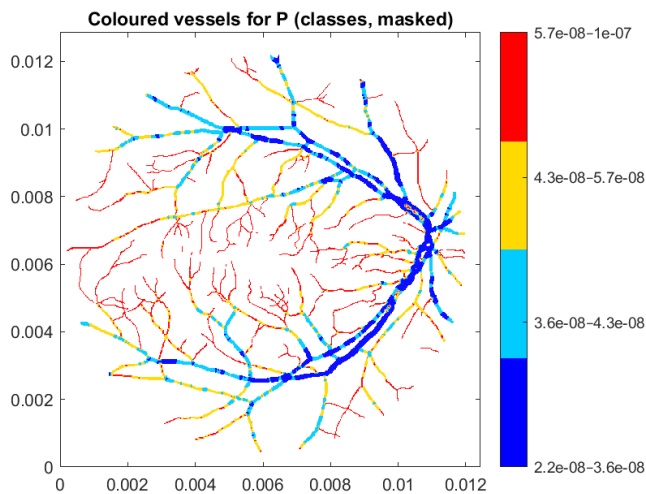


Figure 3 - Building of permeability field

In Figure 4, the histogram of diameters (weighted by border length) showed a right-skewed distribution with a prominent small-diameter peak (fine branches) and a tail toward large trunks; values can be used to sanity-check segmentation.

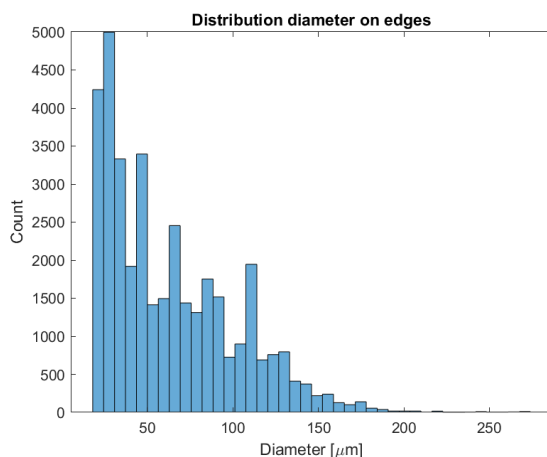


Figure 4 - Histogram of the distribution of diameters

4.1 Geometry-derived maps (radius, permeability, distance)

Starting from the binary fundus, our medial-axis workflow produces a continuous radius map that preserves thin branches while smoothing bifurcation noise; the large trunks appear as long plateaus of nearly constant caliber, whereas distal segments taper progressively. Diameter is then mapped to a vessel-wise permeability field so that major vessels exhibit lower permeability and thin branches higher values, consistent with the phenomenological “thinner → leakier” behavior. A macular ellipse can optionally elevate permeability but only where vessels intersect it, preventing spurious leak in avascular tissue. The distance-to-vessel field defines the supply geometry; after applying the capillary-aware correction (180 μm outside the FAZ and 280 μm within a soft FAZ) the effective exchange distance remains sub-millimetric, avoiding inflated values in vessel-sparse zones. These image-to-physics fields are exported and used directly by the solver. In Figure 5, on the left, this pipeline manifests as a bright perivascular sleeve of albumin concentration at 600 s, with flux arrows oriented predominantly normal to vessel walls and a cooler outer rim where the no-flux boundary and finite diffusion reach limit supply. On the right, at higher magnification, it is shown how adjacent branches with different caliber generate distinct local gradients and flux intensities; the capillary-aware distance confines these gradients to narrow bands hundreds of microns wide, explaining the absence of artificial accumulation in truly avascular gaps.

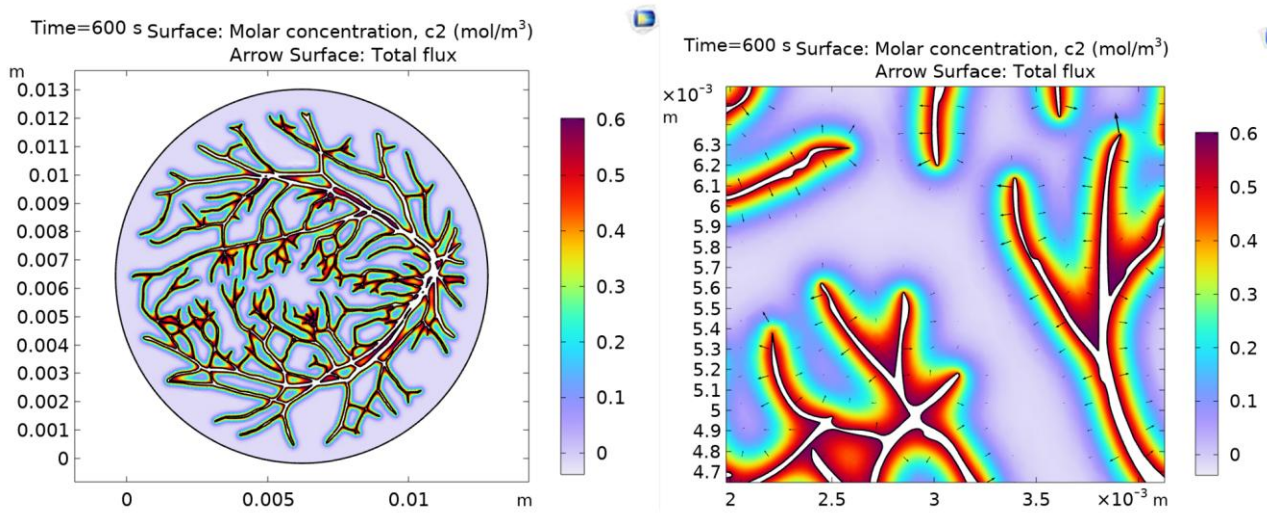


Figure 5 – Molar concentration maps

4.2 Transport simulations (albumin) and dynamic patterns

Time-dependent simulations (0–600 s) with albumin-like effective diffusivity and a modest uniform uptake reproduced plumes emerging from higher-permeability branches and a gradual filling of the parenchyma over the diffusion length (≈ 0.23 mm at 600 s). At early times, concentration remained depressed near the no-flux outer rim, then approached a quasi-steady profile as the domain filled. Using the closest-point projection of wall permeability into the tissue ensured that local driving reflected the nearest vessel segment, which is essential where adjacent branches differ in diameter. In Figure 6, on the left, it is possible to see the plot of D_{eff} that is a constant value, equal to $D_{\text{eff}} = D_0/\lambda^2$, where the tortuosity is $\lambda = 1.6$. On the right, there is the plot of the diffusive flux magnitude that is calculated with Fick’s law. Bright, narrow bands hugging the vessel walls mark regions of steepest concentration gradients; the signal decays over sub-millimetric thicknesses, consistent with both the diffusion length at 600 s and the capillary-aware distance used in the model.

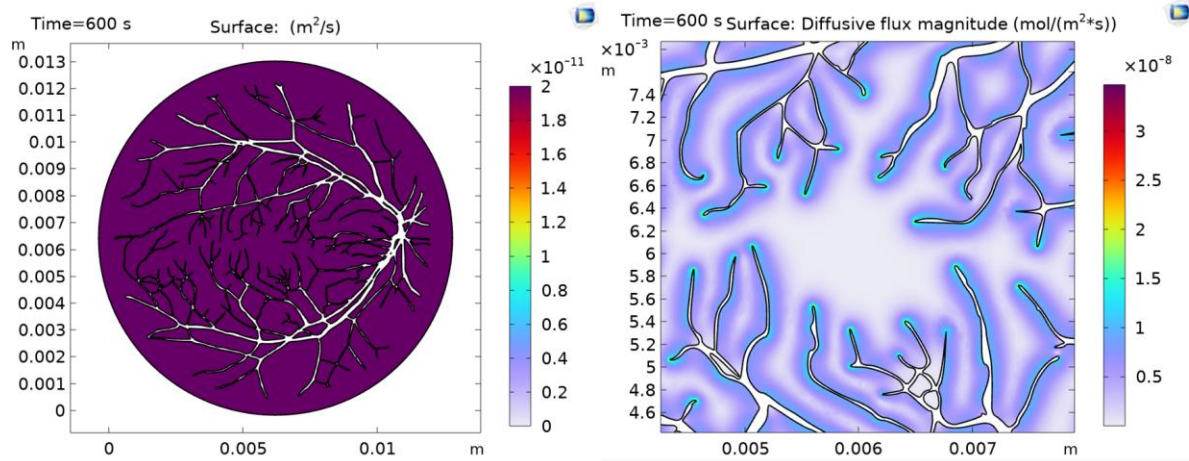


Figure 6 – Diffusivity of the porous matrix and zoom on the diffusive fluxes.

4.3 Structural and dynamic risk maps

The bounded structural risk highlighted regions with longer effective distance and higher local permeability, while remaining lower around thick, low-leak trunks or where uptake dominated. Around the foveal avascular zone (FAZ), our capillary-aware distance permits a slightly larger exchange length than in the perifovea, producing a macula-centered ridge of structural propensity that is visible even when permeability is uniform. When a macular hotspot is enabled—mimicking choroidal/retinal neovascularization (CNV)—the map develops a localized high-risk focus only where vessels cross the macular ellipse, consistent with the vascular origin of leakage and avoiding artefactual signal within the avascular core. Within the context of AMD, the behavior is interpretable as follows: CNV or barrier failure primarily elevates risk by raising permeability, whereas RPE pump impairment or capillary rarefaction effectively increases the exchange distance and shifts the map upward; conversely, anti-VEGF therapy (lower P) or enhanced clearance (higher k) flatten the peaks. With the capillary-aware correction in place, peak risk values stabilize in the 0.3–0.4 range for typical parameter choices, avoiding spurious saturation and yielding macula-centric patterns that are coherent with known AMD pathophysiology (Figure 7).

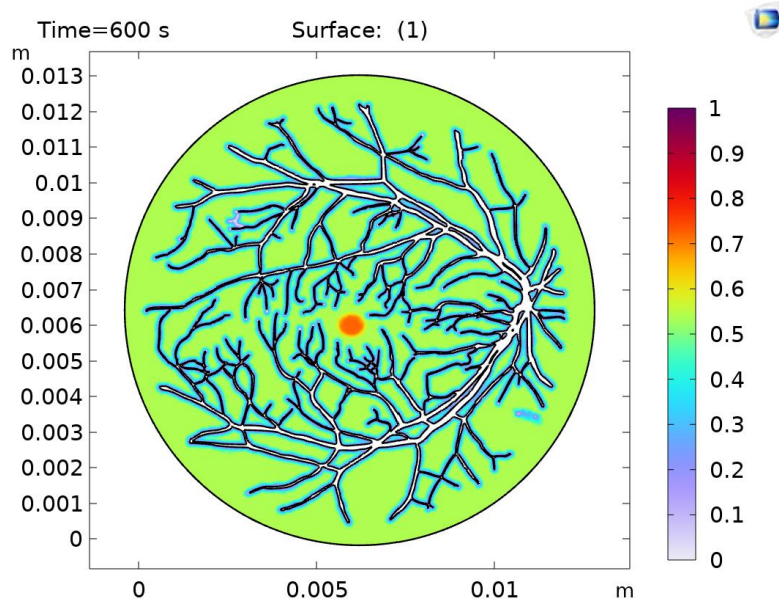


Figure 7 - Risk map

5. Discussion

This work shows that a single segmented fundus can be transformed into quantitative, physics-ready fields—radius, permeability, and exchange distance—and used to drive a forward transport model. In doing so, we bridge routine imaging and biophysical prediction: the fundus ceases to be a static picture and becomes a set of spatial fields that govern diffusion. The pipeline is light, reproducible, and well suited to retrospective studies because it needs only one binary mask per eye. A key ingredient is the capillary-aware exchange distance. Because standard fundus projections omit capillaries, distances computed only to arterioles and venules can reach millimetres, artificially inflating propensity metrics. Capping the distance to physiologic values—tighter outside the foveal avascular zone and looser within it—restores realistic length scales, prevents edge-of-frame artefacts, and stabilizes risk maps. We report two complementary indices: a structural risk that encodes anatomic propensity (geometry and material properties under full supply) and a dynamic risk that further reflects time-resolved availability of solute. The former is useful for baseline comparisons and parameter sweeps; the latter is the appropriate choice for early or transient conditions, clarifying why high-propensity zones may remain benign until the solute arrives. The approach has several strengths—minimal input burden, outputs in physical units that plug directly into COMSOL, vessel-wise heterogeneity via diameter, and interpretable 0–1 maps that facilitate between-eye or longitudinal comparisons—together enabling quantification of vascular-leak heterogeneity without manual labeling, exploration of macular scenarios by moving or resizing a CNV ellipse or tuning permeability, and delivery of individualized boundary conditions to the solver. Limitations include the 2-D projection of a layered organ (out-of-plane effects are collapsed), the absence of intravascular hemodynamics (vessels act as boundary sources), the phenomenological nature of the diameter-to-permeability law, and the dependence on segmentation quality for the smallest branches (partly mitigated by up-sampling and guided smoothing). Future extensions are natural: coupling to pipe-flow or 1-D network models to modulate the blood-side drive, inferring arteriole–venule classes to allow asymmetric permeability, incorporating layer-specific or anisotropic diffusivity from OCT-derived maps, and calibrating permeability, uptake, and diameter sensitivity against dye angiography.

6. Conclusion

We demonstrated a compact, end-to-end pipeline that turns a routine fundus into quantitative boundary conditions and interpretable risk maps for retinal transport. Caliber-derived permeability, a capillary-aware exchange distance, and a closest-point projection from vessel walls to tissue jointly produce stable, physiologically plausible predictions on a 0–1 scale—structural for anatomy, dynamic for time-resolved availability. The method enables scenario testing (e.g., CNV leak), parameter sensitivity (permeability, uptake, capillary scale), and patient-specific comparisons without specialized acquisitions. As such, it offers a practical bridge between clinical images and predictive modeling that can inform hypothesis generation, phenotype stratification, and the design of interventional strategies in AMD and related macular diseases.

Author Contributions

A. Conte conceived and designed the study, performed the analysis and interpretation of the data, drafted the manuscript, and revised it critically for important intellectual content.

F. Boschetti provided supervision and contributed to the critical revision of the manuscript for intellectual content.

Both authors approved the final version of the manuscript and agree to be accountable for all aspects of the work.

Competing Interests

The authors declare that they have no competing interests.

Funding

This work was supported by the European Union – Next Generation EU under the Italian PNRR PhD program, 40th cycle (D.M. 629/2024 and D.M. 630/2024), Mission 4, Component 1.

References

[1] Kaplan HJ. Anatomy and function of the eye. *Chem Immunol Allergy*. 2007;92:4-10. doi:10.1159/000099236

[2] Causin P, Guidoboni G, Malgaroli F, Sacco R, Harris A. Blood flow mechanics and oxygen transport and delivery in the retinal microcirculation: multiscale mathematical modeling and numerical simulation. *Biomech Model Mechanobiol*. 2016;15(3):525-542. doi:10.1007/s10237-015-0708-7

[3] Hoon M, Okawa H, Della Santina L, Wong RO. Functional architecture of the retina: development and disease. *Prog Retin Eye Res*. 2014;42:44-84. doi:10.1016/j.preteyeres.2014.06.003

[4] Goldenberg D, Shahar J, Loewenstein A, Goldstein M. Diameters of retinal blood vessels in a healthy cohort as measured by spectral domain optical coherence tomography. *Retina*. 2013 Oct;33(9):1888-94. doi: 10.1097/IAE.0b013e31829477f2

[5] Wang Q, Kocaoglu OP, Cense B, et al. Imaging retinal capillaries using ultrahigh-resolution optical coherence tomography and adaptive optics. *Invest Ophthalmol Vis Sci*. 2011;52(9):6292-6299. Published 2011 Aug 9. doi:10.1167/iavs.10-6424

[6] Ghassemi F, Mirshahi R, Bazvand F, Fadakar K, Faghihi H, Sabour S. The quantitative measurements of foveal avascular zone using optical coherence tomography angiography in normal volunteers. *J Curr Ophthalmol*. 2017;29(4):293-299. Published 2017 Jul 29. doi:10.1016/j.joco.2017.06.004

[7] Arthur E, Elsner AE, Sapoznik KA, Papay JA, Muller MS, Burns SA. Distances From Capillaries to Arterioles or Venules Measured Using OCTA and AOSLO. *Invest Ophthalmol Vis Sci*. 2019;60(6):1833-1844. doi:10.1167/iavs.18-25294

Appendix

Table A — Image → Physics mapping (MATLAB side)

Name	Symbol / Var	Value (default)	Role	Notes
Image size	$N_x \times N_y$	e.g., 565 × 584 px	Scaling	From the segmented fundus (white vessels on black).
Physical width/height	W, H	0.012–0.013 m	Mapping px→m	Field of view ($\approx 12\text{--}13$ mm for 45° fundus). Used to compute: $\Delta x=W/N_x$; $\Delta y=H/N_y$; $y=H/N_y$.
Vertical flip for COMSOL	—	applied	Orientation	Exported CSVs use bottom-left origin (COMSOL convention).
Upsampling factor	up	1–2 (default 2 if thin branches)	Robust skeleton	Optional; improves stability on very thin segments.
Morphological clean	—	bridge/close (light)	Mask QC	Reconnect 1-px gaps without biasing caliber.
Skeleton smoothing (σ)	sig_skel	1–2 px	Smooth R on skeleton	Averages radius along centerlines; preserves topology.
In-mask smoothing (σ)	sig_vessel	1–2 px	Smooth R in lumen	Guided by vessel mask to avoid spilling across walls.
Radius calibration	γR	1.0 (0.8–1.2)	Bias correction	Optional global scale to match known trunk diameters.

Name	Symbol / Var	Value (default)	Role	Notes
Caliber→Permeability baseline	P_0	1.0×10^{-8} m/s	Leak magnitude	Average A/V leak when no class info is available.
Reference radius	Rref	20 μ m	Law scale	Sets the “neutral” caliber for the P(R)P(R) law.
Slope sensitivity) (caliber α	α	0.6	Law shape	Higher α → stronger contrast (thin branches leakier).
Radius floor	R_min	4 μ m	Robustness	Avoids unrealistically high PP from tiny radii.
Permeability bounds	P_min, P_max	$1e^{-8}$, $1e^{-5}$ m/s	Robustness	Clips extremes in the map.
CNV/hotspot permeability	PCNV	3×10^{-6} m/s	Macular leak	Applied only where vessels intersect the ellipse.
Macula center	(xc, yc)	(W/2, H/2)	Hotspot	Adjustable to patient anatomy.
Macula semiaxes	a, b	1.2, 0.9 mm	Hotspot size	Elliptical region around fovea (soft-edged).
Hotspot rotation	θ	0 deg	Orientation	Optional.
Hotspot softness	sCNV	0.15	Transition	Logistic edge softness of the ellipse.
Distance map export	Lfun(x, y)	CSV (m)	Geometry	Distance outside vessels to nearest vessel wall (flipped).
Permeability export	Pfun(x, y)	CSV (m/s)	Boundary BC	Per-vessel leak field (evaluated on walls in COMSOL).
Radius export	Rfun(x, y)	CSV (m)	Optional	For analysis/verification in COMSOL.

Table B — Transport model & indices (COMSOL side)

Name	Symbol / Var	Value (default)	Unit	Where used	Notes
Domain diameter	—	12–13 mm	m	Geometry	Matches MATLAB $W=H=H$.
Free diffusivity (albumin)	D0	6.0×10^{-11}	m^2/s	TDS	Literature value at 37 °C.
Tortuosity	Λ	1.6	—	TDS	Effective $Deff = D0/\lambda^2 \approx 2.34 \times 10^{-11} D_{\text{eff}} = D0/\lambda^2 \approx 2.34 \times 10^{-11} m^2/s$.
Effective diffusivity	Deff	2.34×10^{-11}	m^2/s	TDS (domain)	Use Deff (or Deff2 if heterogeneous).
Porosity (optional)	E	0.2	—	Porous accumulation	Neutral assumption; not critical if using pure diffusion.
Uptake rate	K	$(5-10) \times 10^{-6}$ (default 1×10^{-5})	s^{-1}	TDS source	Controls Damköhler; adjust to keep risk in 0.3–0.4.
Blood-side concentration	conc	0.6	mol/ m^3	Boundary drive	≈ 0.6 mM serum albumin.
Vessel type	BC —	External convection	—	Boundary (vessels)	Mass transfer coeff = Pwall_eff (see below).

Name	Symbol / Var	Value (default)	Units	Where used	Notes
Permeability function	$P_{\text{fun}}(x, y)$	CSV	m/s	Functions	Interpolation; extrapolation constant (0).
Boundary permeability var	P_{wall}	$P_{\text{fun}}(x, y)$	m/s	Variables (Boundary)	Raw per-vessel permeability.
(Optional) compression/blend	$P_{\text{wall_eff}}$	see below	m/s	Variables (Boundary)	Stabilize map: blend with constant baseline.
Closest-point projection	genext1	search 0.005	m	Coupling	Boundary→Domain to get $P_{\text{near}} = \text{genext1}(P_{\text{wall_eff}})$.
Distance function	$L_{\text{fun}}(x, y)$	CSV	m	Functions	Distance to nearest large vessel (flipped).
Domain height	H	0.012	m	Parameters	For $\text{ell} = L_{\text{fun}}(x, H - y)$ (orientation fix).
Capillary threshold (out FAZ)	$\ell_{\text{cap,out}}$	1.8×10^{-4}	m	Variables	Implicit capillary exchange distance (180 μm).
Capillary threshold (FAZ)	$\ell_{\text{cap,FAZ}}$	2.8×10^{-4}	m	Variables	Larger distance allowed in FAZ (280 μm).
FAZ ellipse center	(x_F, y_F)	(W/2, H/2)	m	Variables	Approx. macula center.
FAZ semiaxes	a_F, b_F	0.35, 0.30	mm	Variables	Typical FAZ footprint.
FAZ rotation	θ_F	0	deg	Variables	Optional.
FAZ softness	s_F	0.15	—	Variables	Logistic edge softness (adim.).
Effective exch. distance	ell_eff	$\min(\text{ell}, \ell_{\text{cap_xy}})$	m	Variables	$\ell_{\text{cap,xy}} \setminus \text{ell_}\text{cap,xy}$ blends out/FAZ thresholds.
Biot number (structural)	B_i	$P_{\text{near}} * \text{ell_eff} / D_{\text{eff}}$	—	Variables	Uses nearest-vessel P and capillary-aware distance.
Damköhler number	Da	$k * \text{ell_eff}^2 / D_{\text{eff}}$	—	Variables	Uniform uptake sink.
Structural risk (bounded)	Risk01	$B_i / (1 + B_i + Da)$	0–1	Variables	Time-independent index.
Dynamic availability	c_{frac}	$\min(1, c / \text{conc})$	$\max(0, \text{---})$	Variables	Fraction of local solute vs blood driver; clamped.
Dynamic risk (bounded)	$\text{Risk01}_{\text{dyn}}$	$\text{Risk01} * c_{\text{frac}}$	0–1	Variables	Time-resolved index (falls near rim at early times).
Diffusion length (optional)	L_d	$4 D_{\text{eff}} t$	m	Variables	If preferring a proxy: $\text{Risk01} * \exp(-(\text{ell_eff} / L_d)^2)$.
Time window	—	0–600 (step 5)	s	Study	Good coverage for albumin spread at D_{eff} above.
Mesh max size	—	20–50 μm	m	Mesh	Target $\leq L_d / 3 L_d / 3$ at final time; refine near walls if needed.